The Multiple-Vortex Structure of the El Reno, Oklahoma, Tornado on 31 May 2013

HOWARD B. BLUESTEIN

School of Meteorology, University of Oklahoma, Norman, Oklahoma

KYLE J. THIEM

National Weather Service, Peachtree City, Georgia

JEFFREY C. SNYDER

NOAA/OAR/National Severe Storms Laboratory, Norman, Oklahoma

JANA B. HOUSER

Department of Geography, Ohio University, Athens, Ohio

(Manuscript received 28 February 2018, in final form 17 May 2018)

ABSTRACT

This study documents the formation and evolution of secondary vortices associated within a large, violent tornado in Oklahoma based on data from a close-range, mobile, polarimetric, rapid-scan, X-band Doppler radar. Secondary vortices were tracked relative to the parent circulation using data collected every 2 s. It was found that most long-lived vortices (those that could be tracked for ≥15 s) formed within the radius of maximum wind (RMW), mainly in the left-rear quadrant (with respect to parent tornado motion), passing around the center of the parent tornado and dissipating closer to the center in the right-forward and left-forward quadrants. Some secondary vortices persisted for at least 1 min. When a Burgers–Rott vortex is fit to the Doppler radar data, and the vortex is assumed to be axisymmetric, the secondary vortices propagated slowly against the mean azimuthal flow; if the vortex is not assumed to be axisymmetric as a result of a strong rear-flank gust front on one side of it, then the secondary vortices moved along approximately with the wind.

1. Introduction

The existence of 1–10-m-scale (i.e., sub-tornado scale) vortices embedded within a larger (100-m–1-km scale) tornado vortex was first postulated based on analyses of airborne photographs of cycloidal damage marks on the ground, which Fujita et al. (1970) initially referred to as ''suction spots'' (highly localized regions of intense upward motion) and later as ''suction vortices'' (Fujita 1981). Following Fujita's pioneering work, many ''multiple vortex'' tornadoes have been observed by storm chasers and the public (e.g., Bluestein 2013), so they are much more common than originally thought. They have been difficult to analyze in nature because the multiple vortices (also known as ''secondary''[1] vortices) are narrow (too small to resolve with most radar systems operating at relatively long ranges), short lived, and difficult, if not impossible, to predict. In many instances, tornadoes may undergo transitions both to and from single- and multiple-vortex structures (e.g., Wurman 2002; Alexander and Wurman 2005; Wurman and Kosiba 2013; Wurman et al. 2014; Bluestein et al. 2015).

Corresponding author: Howard B. Bluestein, hblue@ou.edu

[1] ''Suction vortices,'' ''secondary vortices,'' ''multiple vortices,'' and ''subvortices'' all refer to the same phenomenon: sub-tornado-scale vortices rotating around a larger, parent tornado vortex. In this paper, we will use the second terminology, as first used by Ward (1972, p. 1203). We will not use the sometimes-used terminology here of ''satellite vortices,'' because they refer to tornadoes that are separate from the main tornado vortex (Bluestein et al. 2015).

DOI: 10.1175/MWR-D-18-0073.1

It is well known that for axisymmetric flow in a laboratory tornado chamber or numerical simulation thereof, secondary vortices, which are smaller in horizontal scale than their parent vortex (which in nature is ~100 m–1 km in scale), can occur when the swirl ratio (Lewellen 1962; Davies-Jones 1973) is relatively high (Church et al. 1979; Davies-Jones et al. 2001; Rotunno 2013). The swirl ratio is a measure of the relative amount of azimuthal velocity at the edge of the updraft to the vertical velocity of the updraft in a laboratory chamber or, equivalently, $R(v_0 2\pi R)/(2w\pi R^2)$, where v_0 is the azimuthal wind at the edge of the updraft of radius R, and w is the updraft. When the swirl ratio in the chamber is high, the vortex widens as a central downdraft is forced by a downward-directed perturbation pressure gradient force; a zone of strong lateral shear of the azimuthal wind develops radially inward of the ring of strongest azimuthal wind, which could, for some highly idealized flows, become unstable with respect to small perturbations (e.g., Rotunno 1978; Staley and Gall 1979), such that small-scale vortices develop within the larger vortex and rotate around with the broader-scale flow. Walko and Gall (1984) showed that radial shear of the vertical velocity may also be important for the formation of secondary vortices.

Ward (1972), Forbes (1978), and Rotunno (1984) found from laboratory experiments and numerical-simulation experiments of tornado-chamber-like flow that at the surface, the secondary vortices under highly idealized conditions propagate against the azimuthal flow at about half its speed. Walko and Gall (1984; their Table 1) also found that secondary vortices may propagate against the mean flow. This behavior is reminiscent of Rossby waves in a vortex,[2] which propagate against the main flow when the radial gradient of potential vorticity is directed toward the center of the parent vortex. In a vortex, the radial gradient of vorticity must be from radial gradients in the basic-state azimuthal wind. If there is solid-body rotation, there is no radial gradient in vorticity, so Rossby waves are not possible. However, in a Rankine-combined vortex (Rankine 1882; Davies-Jones 1986), there is a radial gradient in vorticity that is directed toward the center of the parent vortex at the radius of maximum wind (RMW), beyond which there is zero vorticity; Rossby waves are possible there or beyond the RMW if the azimuthal winds drop off with radius rapidly enough that vorticity does not vanish beyond the RMW and so decreases with radius. In addition, unlike Rossby waves, it has been shown that the radial and vertical gradients of vertical velocity and viscosity may play significant roles in producing secondary vortices in addition to the radial shear of the azimuthal wind (e.g., Nolan 2012).

Lewellen et al. (2000) noted that other parameters also affect the vortex structure near the ground, indicating that flows that have the same swirl ratio can produce different corner flow characteristics. They suggested that the "corner flow" swirl ratio (the ratio of the azimuthal flow in the core of the vortex, near the ground, to the radial inflow) better characterizes the vortex structure near the ground. Although estimates of swirl ratio in mesocyclones and tornadoes in nature have been made with airborne and ground-based mobile Doppler radars (Wakimoto and Liu 1998; Lee and Wurman 2005), whether the wind measurements actually represent the flow parameters described by the swirl ratio in idealized vortex chambers is not clear, and there are significant uncertainties in the estimates of the wind variables. Furthermore, measurements when the tornado has both single- and multiple-vortex structures during its lifetime are needed for comparison to see if the swirl ratio as it is estimated does indeed increase when the tornado changes from a single-vortex structure to a multiple-vortex structure, and vice versa.

Unlike in vortex chambers and idealized simulations, tornadoes produced in nature by supercells are not embedded in a homogeneous environment because cooler air from an adjacent region of precipitation may be advected around the parent mesocyclone (e.g., Marquis et al. 2012; Rotunno 2013; Beck and Weiss 2013; Weiss et al. 2015); flow associated with a strong rear-flank gust front can also add to the nonhomogeneity of the near-tornado environment. The rear-flank downdraft and secondary, internal surges may be driven by negative buoyancy associated with the evaporative cooling and melting of descending hydrometeors or by dynamical processes (e.g., Skinner et al. 2014). In addition, tornadoes have a component of translational motion along with their parent storms (e.g., Fujita et al. 1970), so the ground-relative wind field is not axisymmetric.

Since tornadoes and especially sub-tornado-scale vortices can be very damaging, they are most safely studied in nature by using remote sensing techniques. Mobile Doppler radars have occasionally resolved the multiple-vortex structure of some tornadoes and mesocyclones (Wurman et al. 1997; Wurman 2002; Lee and Wurman 2005; Alexander and Wurman 2005; Wurman et al. 2014; Wakimoto et al. 2015) and even dust devils (Bluestein et al. 2004a). In addition, some finescale measurements along the inner edge of the weak-echo hole (WEH) or

[2] Vortex Rossby waves have been studied in tropical cyclones (e.g., Schubert et al. 1999; Reasor et al. 2000; Terwey and Montgomery 2002).

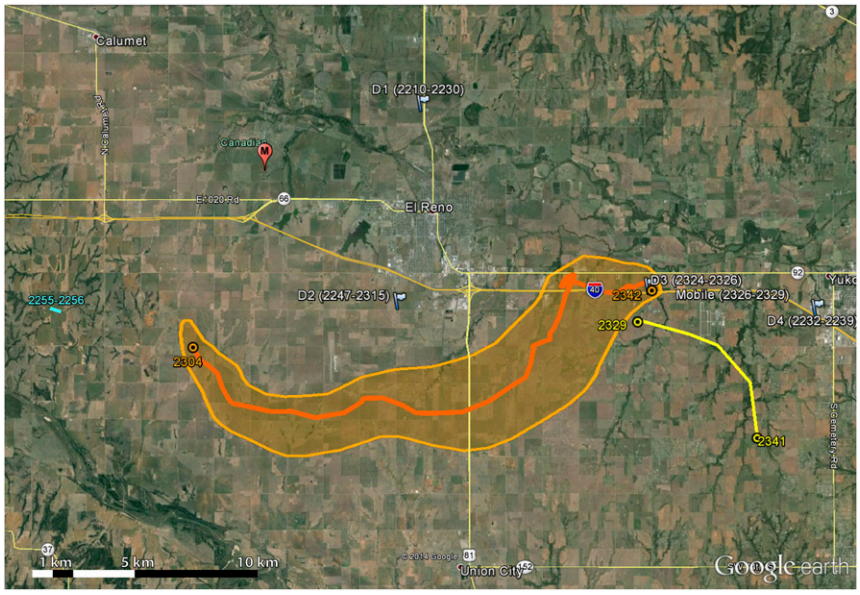

FIG. 1. Tracks of three of the nine tornadoes in the El Reno, OK, supercell, on 31 May 2013 from Bluestein et al. (2015; their Fig. 8). D1–D4 are deployments 1–4 during the times indicated in UTC. The times of each of three tornadoes are indicated at the beginning and end of each track. [The red pin "M" is the location of a mesonet site discussed in Bluestein et al. (2015), but not here.]

"eye" (e.g., Wurman and Gill 2000; Bluestein and Pazmany 2000; Wakimoto et al. 2011; Tanamachi et al. 2012) have shown periodic undulations in reflectivity (Bluestein and Pazmany 2000), which may also be indicative of waves embedded within the azimuthal flow.

Since sub-tornado-scale (secondary) vortices usually do not appear to last very long (tens of seconds or less), it is difficult to document their evolution and motion using conventional, mobile Doppler radars, which can take 2 min or longer to scan a volume containing a tornado and a portion of its parent storm (e.g., Markowski et al. 2012). However, rapid-scan radars (Wurman and Randall 2001; Bluestein et al. 2010; Pazmany et al. 2013; Kurdzo et al. 2017) can provide volume scans with an update time as short as 5–15 s. Rapid-scan, X-band, polarimetric radar (RaXPol) can provide updates at one elevation angle every 2 s (Pazmany et al. 2013).

On 31 May 2013, a violent tornado was observed near El Reno, Oklahoma (Seimon et al. 2016), and probed by several mobile Doppler radars (Wurman et al. 2014; Bluestein et al. 2015; Wakimoto et al. 2015; Thiem 2016). This tornado, which was one of nine that formed from the same parent supercell, at times exhibited multiple-vortex structure that was visible as multiple condensation funnels (Bluestein et al. 2015; Seimon et al. 2016). In particular, the evolution of secondary vortices was documented by RaXPol, which provided scans at low levels at the unprecedented rate of once every 2 s, thus allowing one to track individual vortices for several scans or more (Snyder and Bluestein 2014) and, in turn, reducing the possibility of temporal aliasing that may occur when the update time is longer. The short update time is the shortest for any multiple-vortex tornado in any existing rapid-scan mobile Doppler radar dataset.

The primary purpose of this paper is to describe the evolution of some of the secondary vortices and their environment using data from RaXPol, which began data collection prior to tornadogenesis and continued through the multiple-vortex stages of the tornado (Snyder and Bluestein 2014; Bluestein et al. 2015). Details of RaXPol's characteristics, the methods employed to analyze the data, and deployment locations with respect to the tornado are given in section 2. An analysis of the tracks of the secondary vortices is described in section 3. Section 4 contains a discussion of the secondary vortices related to the larger-scale background flow. A summary of our findings and conclusions is found in section 5.

2. Data analysis

Details of field operations on 31 May 2013 are given in Bluestein et al. (2015), and technical details about RaXPol are given in Pazmany et al. (2013). Some information relevant to the field operations and data discussed in this study is reproduced in Fig. 1 and Table 1.

This study concerns itself with the third deployment of the day (D3), when secondary vortices were resolved within the second tornado produced by the

TABLE 1. Characteristics of RaXPol.

	RaXPol
Operating frequency	9.73 GHz ± −20 MHz
Antenna diameter	2.4 m
Antenna 3-dB beamwidth	1.0°
Dwell time	Usually chosen to be equivalent to 1° per radial
Azimuthal rotation rate	Up to 180° s^{-1}
Peak power (H + V)	20 kW
Pulse width	0.5–40 μs
Range resolution	15–150 m
Gate spacing	7.5–75 m
31 May 2013 scanning strategies before and during El Reno tornado	
D3 (2324–2329 UTC)	0°–5° every 1°
In motion after 2326 UTC	30-m-range resolution, 15-m gate spacing

parent supercell (Bluestein et al. 2015). Although secondary vortices and even a satellite vortex were detected at other times, we restrict ourselves to the time period from 2324:01 to 2326:11 UTC (LDT is 5 h earlier), when the secondary vortices were ubiquitous; D3 was short owing to the approaching violent tornado, and the radar truck continued to collect data as it moved to the next deployment location. During D3, the tornado was located ~3.5–5.5 km to the southwest of the radar.

The half-power beamwidth of RaXPol's 2.4-m-diameter parabolic dish antenna is 1°. The antenna is rotated rapidly at the rate of 180° s^{-1}, which results in beam smearing of about 0.4°–0.5° (Doviak and Zrnić 1993; Pazmany et al. 2013). This smearing could have been eliminated by use of a "strobe mode," but this mode was experimental in 2013, and we were hesitant to use an experimental mode of transmission while a very large tornado was nearby. Since the rotation rate is so rapid, pairs of pulses were transmitted at 11 different frequencies separated by a pulse bandwidth (at 9.73 GHz ± 20 MHz) so that enough quasi-independent samples could be obtained to yield what are considered to be low-variance estimates (e.g., Doviak and Zrnić 1993; Bringi and Chandrasekar 2001; Snyder and Bluestein 2014). For a few minutes, data were collected with only 30-m-range resolution with a 15-m-range gate spacing (due to oversampling), during which time only eight pulses were used, which is considered suboptimal for computing radar moments. However, in tornadic debris, decorrelation times are comparatively short; data from the horizontal and vertical channels are poorly correlated, so data from each channel may be averaged to increase the number of samples used to compute the Doppler velocity (Snyder and Bluestein 2014). At 5–7.5-km range, where most of the radar measurements were made, the smeared azimuthal resolution was ~125–200 m, with the dwell time between radials chosen to be equivalent to 1° per radial.

Although the 20-kW transmitted power of the radar was sufficient to detect precipitation and debris motion at the range of the radar from the tornado, some regions, especially in clear air, were noisy enough that data had to be discarded. Data were manually edited to remove ground clutter and obvious noise using the third version of SOLO (Oye et al. 1995). Additional data were discarded if the normalized coherent power (NCP) (Uttal and Intrieri 1993; Wurman and Gill 2000; Friedrich and Hagen 2004; Wurman et al. 2007a), also known as the signal quality index (SQI) (Schroth et al. 1988; Friedrich and Hagen 2004; Friedrich et al. 2006), was less than 0.2 (e.g., Friedrich and Caumont 2004; Wurman et al. 2007a; Snyder and Bluestein 2014). The NCP is inversely related to the spectrum width (Friedrich and Caumont 2004; Friedrich and Hagen 2004; Friedrich et al. 2006), which was computed as in Doviak and Zrnić (1993). The removal of noisy data (see the appendix for more details) was particularly important for the case described herein because the detection and tracking of secondary vortices required particular care.

Because the pulse repetition time was 0.25 ms, there was velocity aliasing at 31 m s^{-1}, which at times was merely ¼ of the actual Doppler velocity. The Doppler velocity data were unfolded using dealiasing algorithms in regions where the Doppler velocity spatial gradients were relatively weak. In regions near and within the tornado, where there were strong gradients, data were manually dealiased.

Secondary vortices were identified subjectively as a velocity couplet, consisting of a local minimum and local maximum in Doppler velocity, located adjacent to one another with a difference of at least 40 m s^{-1} (Fig. 2). This criterion has been applied by others to tornadic vortices (e.g., Alexander and Wurman 2008; Alexander 2010; Marquis et al. 2012; Kosiba et al. 2013). Furthermore, there had to be temporal continuity for at least three successive plan position indicator (PPI) scans, each of which took ~2 s. In three successive PPI scans the elevation change is ~250–300 m. Each full volume scan (from 0° to 5° elevation angle, every 1°) took ~15–16 s. The 40 m s^{-1} criterion is justified on the basis of the minimum damage inflicted from the extent of damage observed: if a tornado is stationary, then a ground-relative wind speed of 20 m s^{-1} could produce minimal damage on the basis of the Fujita (F) scale (Fujita 1981), for which the minimum threshold is 18 m s^{-1}. However, for a more accurate representation of operational cases, a storm motion magnitude on the order

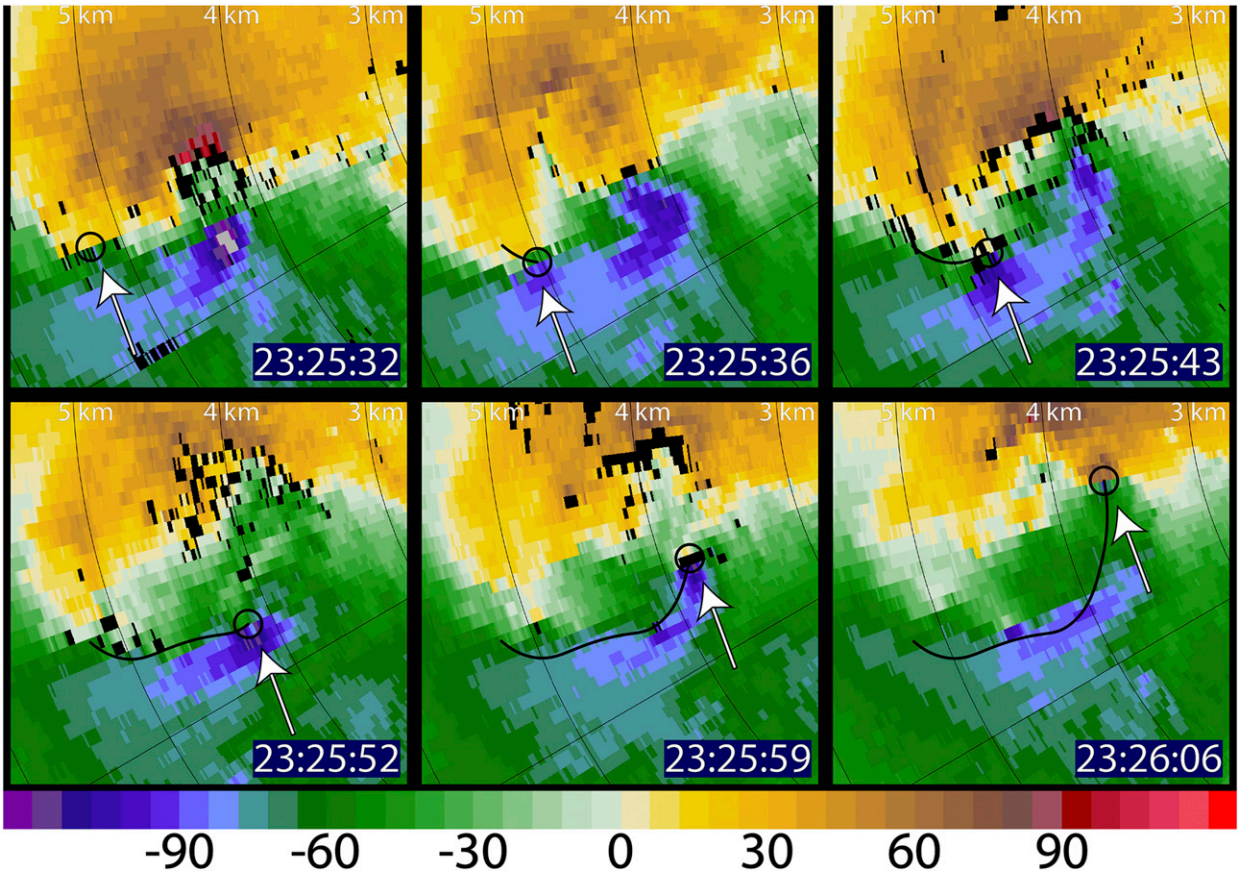

FIG. 2. The track (curved black line) of a secondary vortex from 2325:32 to 2326:06 UTC (at elevation angles of 3°, 5°, 1°, 5°, 1°, and 4°, respectively; the approximate altitude at 1°, 3°, 4°, and 5° is 79, 236, 314, and 393 m, respectively), 31 May 2013 in the El Reno, OK, tornado. Dealiased RaXPol Doppler velocity color is coded in m s^{-1}; range markers are shown every 1 km. Locations of cyclonic vortex signature indicated (pointed to by white arrows) by circles.

of ~10 m s^{-1} added to the ground-relative winds could produce minimal damage on the basis of the more recent enhanced Fujita (EF) scale (WSEC 2006), for which the minimum threshold is 29 m s^{-1}.

Some numerical simulations indicate that secondary vortices in idealized models of tornadoes are not tilted above the surface friction layer (Nolan 2013), even though they sometimes appear to be tilted right near the ground both in simulations and in nature (Fig. 3). If it is assumed that secondary vortices are not significantly tilted with height below the maximum height scanned by the radar (~450 m AGL for dataset discussed here) and above the surface friction layer, which is probably not well resolved, then the location of each secondary vortex can be tracked every 2 s; Wurman (2002) successfully used this technique with data collected in a small sector every 4–5 s. If the subsequent location of the vortex signature appears to be continuous within volume scans and across successive volume scans (i.e., if there is no jump in location between the highest-elevation scan and the lowest-elevation scan in the following sequence), then it is very likely that a unique secondary vortex is being tracked and that errors due to tilt are negligible. The availability of rapid-scan radar data is therefore crucial in allowing one to track secondary vortices, even more so than it is for resolving tornadogenesis (Wurman et al. 2007b; Bluestein et al. 2010), because from film and videos of multiple-vortex condensation funnels, they appear to last for only a number of seconds at most (not shown). While it may be faster and easier to use an automatic algorithm (e.g., Potvin 2013) for tracking each secondary vortex, in this study, the first for which rapid-scan data were used to track secondary vortices, it was deemed prudent to be as careful as possible, even if the process were much more painstaking.

Since subjectively determined tracks contain some noise, it was necessary to apply some smoothing. An ellipse was fitted to the core of the tornado, just inside the RMW, and the center of the ellipse for each time step represented the estimated center of the tornado at

FIG. 3. Photos of secondary vortices showing both tilted and nontilted condensation funnels. (a) Friendship, OK, 11 May1982; (b) Verden, OK, 3 May 1999; (c) eastern Texas Panhandle, 22 Apr 2010; (d) El Reno, OK, 31 May 2013; (e) Chickasha, OK, 6 May 2015; and (f) Dodge City, KS, 24 May 2016. All photographs courtesy of H. Bluestein. Many of the secondary vortices lean radially outward with distance from the center of the parent circulation. In others, it is not possible to determine any tilt, though there could be tilt along the line of site, which is not evident. In the rest, the tilt may be normal to the field of view.

that particular time. Because of rapidly evolving asymmetries within the vortex's structure, the tornado's location at each time step was smoothed based on an approximate Gaussian weighting function using the tornado's locations during the surrounding time steps. The weight applied to the location of the surrounding time steps was given by

$$f(x) = \alpha \times \exp\left(-\frac{x^2}{2\sigma^2}\right),$$

where $\alpha = 1/\sigma\sqrt{2\pi}$, $\sigma = 27/7\sqrt{2\pi}$, and x is the number of time steps away from the location being adjusted for $x = 0$, 1, 2, and 3.

There have been many studies of tornado structure using the ground-based velocity track display (GBVTD) method (e.g., Lee and Wurman 2005; Tanamachi et al. 2007; Wakimoto et al. 2012; Tanamachi et al. 2013; Kosiba and Wurman 2013). This method, however, was not amenable to the analysis of the multiple-vortex phase of the El Reno tornado considered here, mainly for the following two reasons. First, the flow field was not circularly symmetric (i.e., axisymmetric in the reference frame of the tornado), as required by the technique (Lee et al. 1999); in fact, it highly deviated from circular symmetry. Second, it was not known how badly centrifuging of precipitation and debris in the tornado had

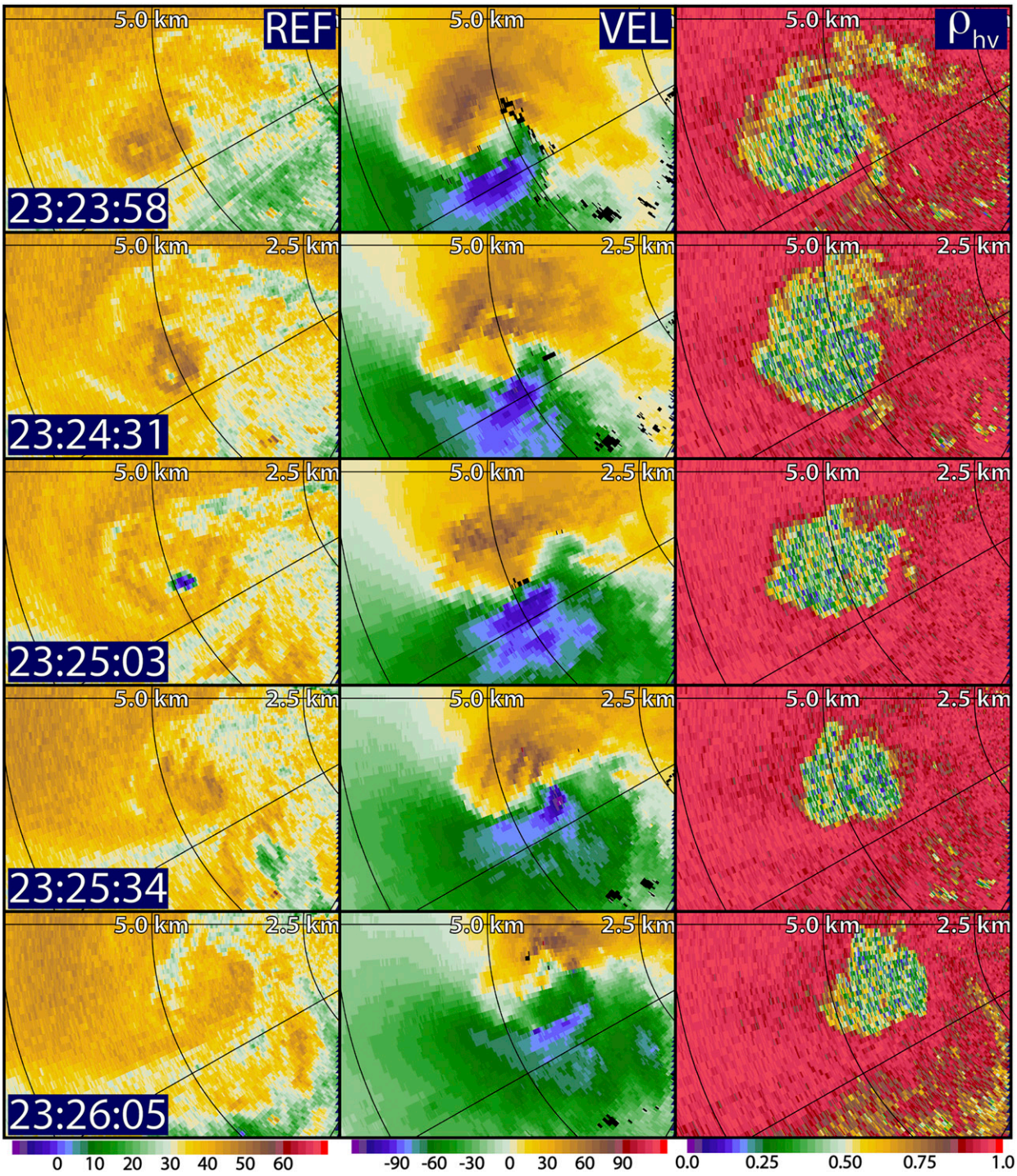

FIG. 4. RaXPol data every ~32 s, at 4° elevation angle, covering the time period when the tornado changed from a single-vortex structure to a multiple-vortex structure, on 31 May 2013, near El Reno, OK, at the times in UTC indicated. (left) Radar reflectivity in dBZ, (middle) dealiased Doppler velocity (m s^{-1}), and (right) copolar cross-correlation coefficient, with the respective color scales shown at the bottom of each column. Range rings are displayed every 2.5 km.

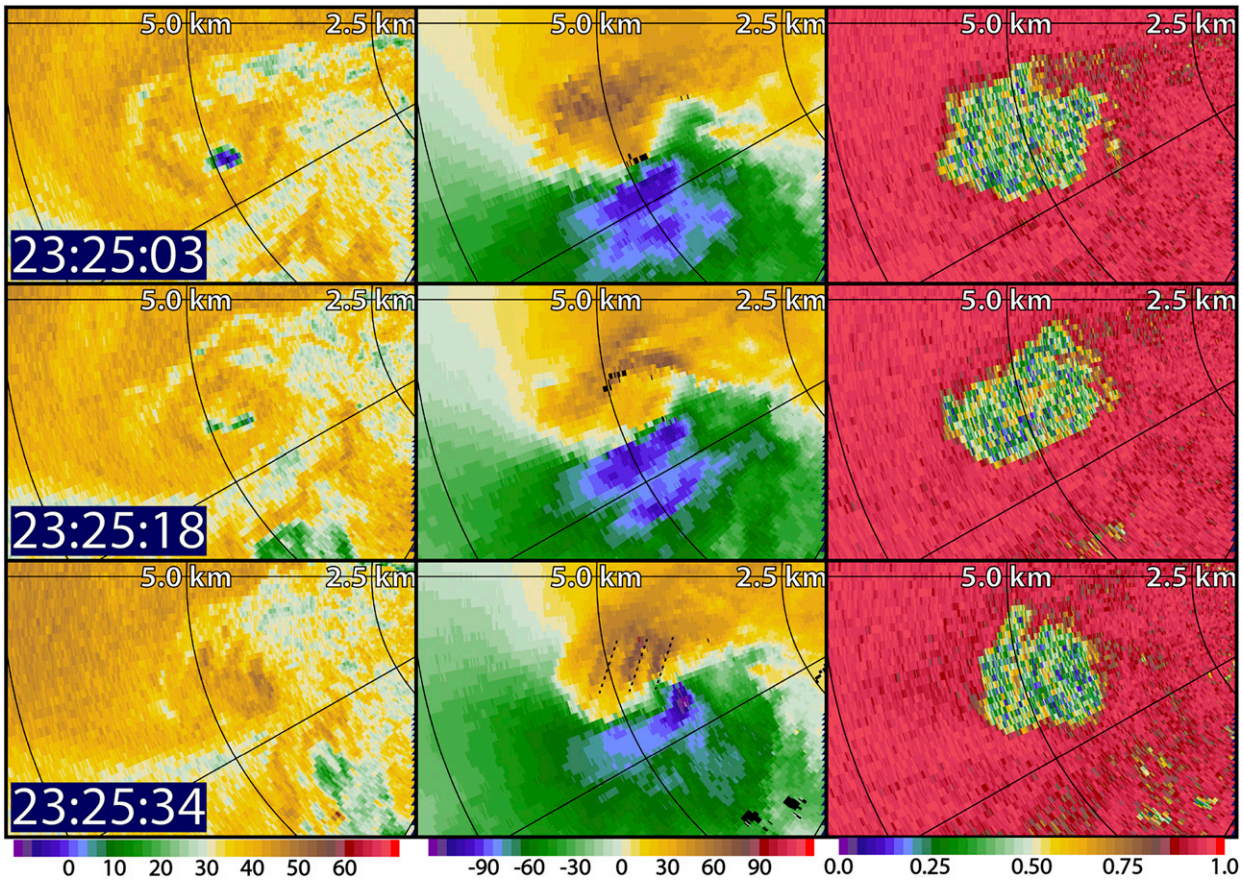

FIG. 5. As in Fig. 4, but for the times of the transition, every ~15–16 s. Dashed line segments indicate approximate location of bands of enhanced radar reflectivity.

corrupted the signal, so the Doppler velocities measured by the radar were not entirely representative of the actual wind (e.g., Nolan 2013). Although it is possible to include the effects of centrifuging using a simple parameterization based on reflectivity (Wakimoto et al. 2012; Kosiba and Wurman 2013) or polarimetric variables [by relating them to specific types of hydrometeors; e.g., Ryzhkov et al. (2005)], there is still a high uncertainty about the exact size, density, and mass of the scatterers. For these reasons, it was decided to estimate the properties of the mean azimuthal flow of the background tornado using a simpler, though also flawed, method, to be described later.

3. The tracks of the small-scale (secondary) vortices

The radar reflectivity, Doppler velocity, and copolar cross-correlation coefficient (ρ_{hv}) fields associated with the tornado vortex at low altitude (~250–300 m AGL) as it was evolving from a single-vortex structure to a multiple-vortex structure over ~2 min is shown in Fig. 4 at ~30-s intervals. At 2323:58 UTC, there was a cyclonic Doppler velocity couplet and a WEH. At 2324:31 UTC, while the WEH was still evident, the Doppler velocity field was no longer characterized by a simple, relatively symmetric, Doppler velocity couplet; instead, the Doppler velocity field was characterized by more than one adjacent maximum in outbound and inbound velocities. At 2325:03 UTC, the primary WEH was becoming elongated in the east (E)–west (W) direction. The WEH broke up into two smaller WEHs by 2325:18 UTC and then had disappeared entirely by 2325:34 UTC (Fig. 5), when a multiple-vortex structure was more apparent. It is thought that a WEH in a tornado above the surface friction layer is created by the outward centrifuging of precipitation particles lofted in the tornado vortex (e.g., Dowell et al. 2005) and that the appearance of a WEH aloft as weak-echo column (WEC) could be caused by strong updrafts (Tanamachi et al. 2012). Thus, the disappearance of a WEH could mean that the intensity of the vortex had decreased

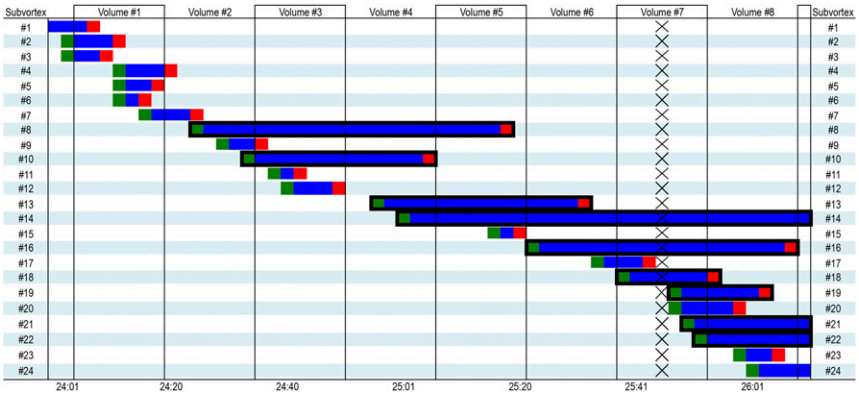

FIG. 6. The times (UTC) on 31 May 2013 of all the secondary vortices (1–24) identified during D3 by RaXPol volume scan number (from one to six). Formation, the period in between formation and dissipation, and dissipation are shown in green, blue, and red, respectively. The formation (dissipation) times were determined to be when the Doppler shear first reached or exceeded 40 m s^{-1} (fell below 40 m s^{-1}). Long-lived secondary vortices are highlighted by a thick black line surrounding the timeline. The ×s denote a time when data were missing, most likely owing to a processing error.

significantly, that the flow field had become asymmetric about the center of circulation, or that there was a transition from a central, single updraft (one-cell vortex) to a central downdraft. Wavelike features of unknown origin at 2325:34 UTC (Figs. 4, 5) were evident in the radar reflectivity field and the outbound portion of the Doppler velocity field; there were three main, parallel bands of enhanced radar reflectivity and outbound Doppler velocity with a wavelength of ~400 m. The maxima in radar reflectivity were located close to the minima in receding Doppler velocity (marked on the Doppler velocity panel of Fig. 5 for 2325:34 UTC), where there were bands of divergence associated with the radial component of the wind. There is thus some evidence that the bands of enhanced reflectivity were associated with bands of vertical motion. By 2326:05 UTC (Fig. 4), there was no WEH, but the cyclonic Doppler velocity couplet was better defined (i.e., had less asymmetry).

The field of low ρ_{hv} (indicative of the debris field; e.g., Ryzhkov et al. 2005; Bluestein et al. 2007b) initially was quasi-axisymmetric about the vortex center, but it soon became elliptically shaped and then more complex, although spiral bands were noted at most times. It is thought that these spiral bands may have been caused by debris ejections (Kurdzo et al. 2015; Houser et al. 2016). Alternatively, it is also possible that they may have been caused by debris falling out outside the core of the tornado and then being advected and deformed into spiral bands by the convergent, cyclonic wind field associated with the tornado, in a manner similar to that described by Moon and Nolan (2015) for spiral bands of radar reflectivity in tropical cyclones.

Twenty-four vortices were tracked over a 2-min period (Fig. 6). The secondary vortices were divided up into 15 ''short-lived'' vortices, which could be tracked for up to 15 s, and nine ''long-lived'' vortices, which could be tracked for at least 15 s. This subdivision was done so that it could be ascertained if vortices that persisted for relatively few scans, lasting for less than 15 s, behaved any differently from those that persisted for more scans, lasting for at least 15 s. In other words, we sought to determine if the more stable vortices behaved differently than the more transient vortices. The two longest-lived vortices lasted ~1 min or longer; one was continuing at the time data collection was terminated and most likely existed longer than the 72 s for which it was recorded.

Since the tracks of the secondary vortices during D3 in a ground-relative reference frame (Fig. 7a) appear continuous, it is thought that any errors resulting from the vortices being tilted with height are small, and tracking vortices in every PPI at successive elevation angles from volume scan to volume scan, especially from the highest-elevation scan to the subsequent lowest-elevation scan, is a valid procedure. The tracks were then subjectively smoothed to account for some error in determining their exact locations.

4. The behavior of the secondary vortices in relation to the larger-scale flow

In addition to tracking the secondary vortices in a ground-relative reference frame (Fig. 7a), the secondary vortices were also tracked in the reference frame of the larger-scale tornado (Fig. 7b) in order to document the

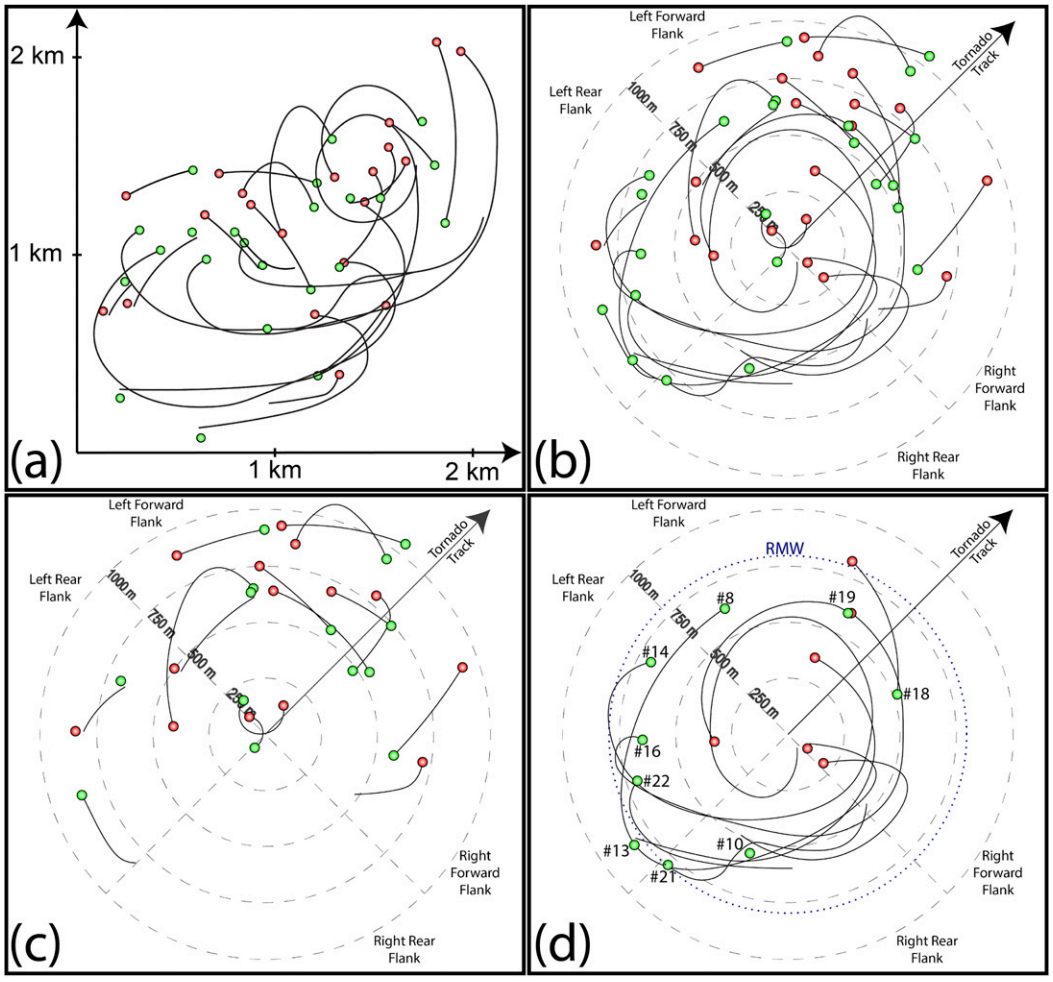

FIG. 7. The smoothed, subjectively identified RaXPol tracks of all the secondary vortices during D3 (a) in a fixed coordinate system; (b) the reference frame of the parent tornado circulation; (c) as in (b), but for the short-lived vortices; and (d) just for the long-lived vortices. The green (red) dots indicate locations of multiple-vortex formation (dissipation). Dots are not shown when the vortices began or ended before or after the data collection times, respectively. In (d), the dotted circle marks the RMW, and the secondary vortex numbers (Fig. 6) are plotted at the formation locations.

behavior and evolution of the small-scale vortices with respect to the center of the parent tornado circulation. Determining the center and flow characteristics of the larger-scale, tornadic flow was difficult owing to the asymmetry and other complexities of the flow (e.g., from the secondary vortices themselves). The asymmetry in the Doppler velocity field is illustrated in Fig. 8, which shows one main outbound isodop maximum and two inbound isodop minima, with substantial small-scale, along-radial variations in Doppler wind velocity. The vortex signature of the mean[3] flow contained a maximum in inbound velocities of $\sim 100\,\mathrm{m\,s^{-1}}$, while the maximum outbound velocities were only $\sim 60\,\mathrm{m\,s^{-1}}$ (Fig. 9a). Even with a translational motion toward the radar of $\sim 10\,\mathrm{m\,s^{-1}}$ (the translational motion varied with time and even ceased for a short interval when a loop was executed; Wakimoto et al. 2015), the flow was still highly asymmetric, with a much stronger inbound flow (by $\sim 20\,\mathrm{m\,s^{-1}}$) compared to the outbound flow. This asymmetry was probably associated with strong flow in the rear-flank downdraft behind the rear-flank gust front (Fig. 8) that biased inbound Doppler velocities even more than what would be expected from the translation of the vortex alone, although there could have been a dynamically induced wavenumber-1 component in the parent tornado as well. When combined with the very

[3] The median dealiased Doppler velocities were used to compute the "mean" flow so that outliers would not bias the results.

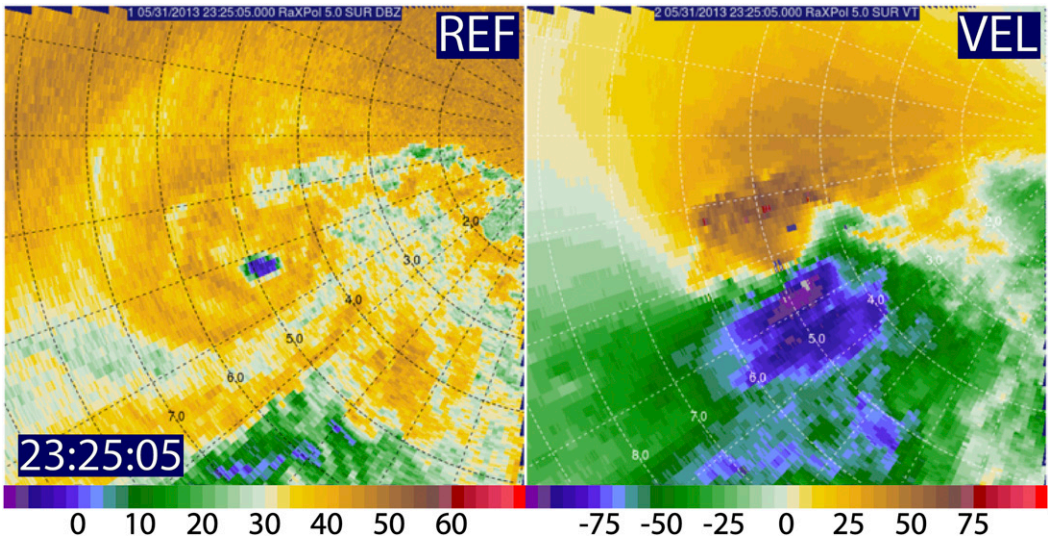

FIG. 8. Asymmetry in the tornado wind field: (a) radar reflectivity field in dBZ and (b) dealiased Doppler velocity ($m\,s^{-1}$) at 2325:05 UTC 31 May 2013, during D3, from RaXPol. Range rings are shown every 1 km. Altitude is ~400 m AGL.

large RMW relative to the azimuthal resolution of the radar at the range of the tornado (i.e., at least 10 radials sample the flow within the RMW), there was no easily identifiable Doppler velocity couplet that could be used to locate the center of the tornado circulation in many individual scans.

The tracks of the secondary vortices with respect to the center of the parent tornado/circulation were erratic and asymmetrical about the center; many vortices approached the center, while some others moved away (Fig. 7b). Most of the vortices originated between 500 and 750 m from the center of the parent tornado circulation (Fig. 10). The characteristics of the tracks exhibited some variations by quadrant with respect to the tornado-motion vector. For example, the tracks of secondary vortices found in the left-forward quadrant were mostly located beyond 500 m from the center of the parent tornadic circulation, while secondary vortices found in the right-forward and right-rear quadrants were mostly located around 500 m from the center of the

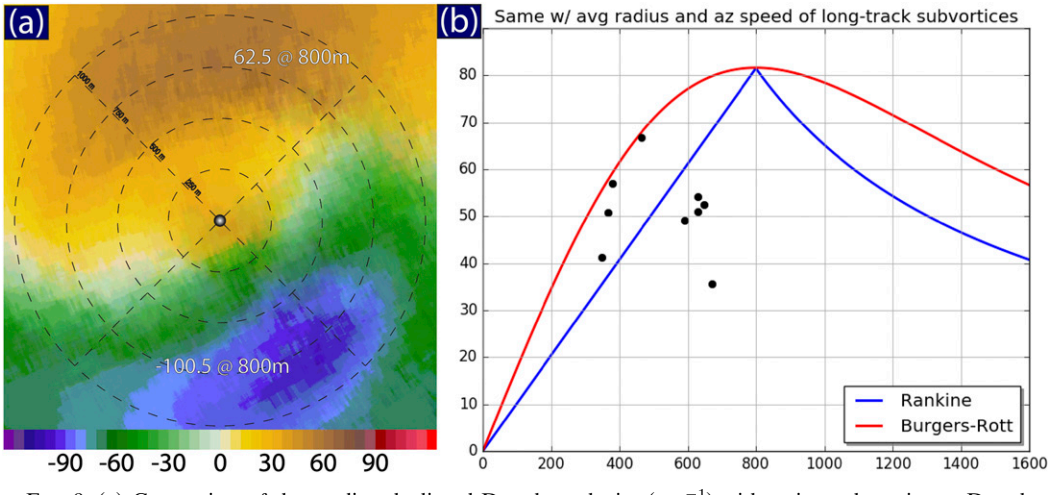

FIG. 9. (a) Composites of the median dealiased Doppler velocity ($m\,s^{-1}$) with estimated maximum Doppler velocities ($m\,s^{-1}$) and RMW (m) noted. (b) Rankine-combined vortex (blue) and Burgers–Rott vortex (red) fit to the estimated azimuthal wind speeds in a coordinate system moving with the parent tornado; mean azimuthal speeds of each long-lived secondary vortex are plotted as black dots. Abscissa [distance from center (m)] and ordinate [Doppler velocity ($m\,s^{-1}$)].

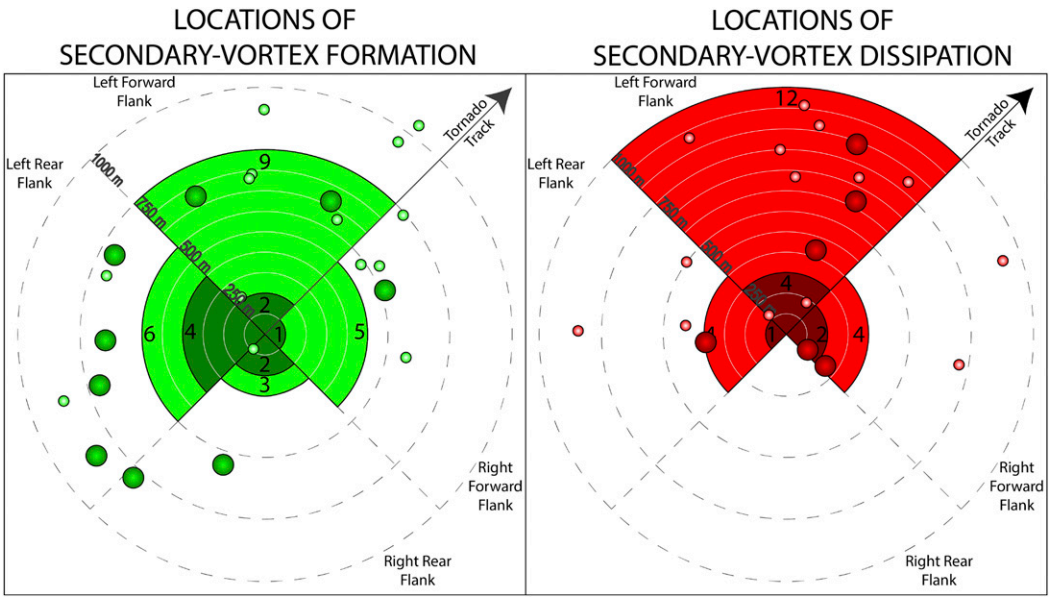

FIG. 10. Polar histograms by quadrant for the number of (left) secondary-vortex formation events and (right) dissipation events and the locations of the former (green circles) and latter (red circles); the darker and larger green (red) circles denote the formation (dissipation) locations of the long-lived (short lived) secondary vortices. In each quadrant, the total number of events (number of long-lived events only) is plotted on the outside (inside) of the histogram for all events (long-lived events).

parent circulation. Half of the short-lived secondary vortices originated in the left-forward quadrant, well over half of the short-lived secondary vortices also dissipated in the left-forward quadrant, and essentially no short-lived secondary vortices were found in the right-rear quadrant, indicating that vortices found within this quadrant were able to sustain themselves until they passed through this area of the parent circulation (Figs. 7c, 10). On the other hand, most of the long-lived secondary vortices (six of nine) formed in, or very near, the left-rear quadrant (Figs. 7a, 10a), and all but one dissipated in one of the forward quadrants (Figs. 7b, 10b). In addition, the tracks of eight of the nine long-lived vortices ended closer to the center of the parent tornado circulation than where the tracks originated (Fig. 7d). Overall, the long-lived vortices tended to form in the left-rear quadrant, rotate around the center of the parent tornado, and dissipate in the right- or left-forward quadrants closer to the center of circulation of the tornado. These tracks of the vortices bear some similarity to the swaths of high wind in some of the numerical simulations of tornadoes by Dahl et al. (2017; their Fig. 2). Many of the tracks of the long-lived secondary vortices overlapped each other, especially in all quadrants except the left-front quadrant. It may be inferred from this finding that particular locations around the parent tornado circulation were supportive of the formation and sustainability of the secondary vortices, while other locations were not, though the limited size of this sample prevents us from stating this more definitively.

An overall statistical analysis of the behavior of the secondary vortices is found in Table 2. More attention should be given to the behavior of the long-lived vortices because they were easier to track (and thus, less prone to errors associated with the short, but not short enough, 2-s update time) and analyze relative to the less-consistent nature of the short-lived vortices. For all secondary vortices whose entire life span was captured during D3 (i.e., not including those that began before or ended after D3), the average lifetime was 16 s, and the average pathlength was 860 m. Scanning rates of at least once every 8 s may, therefore, be required to track most secondary vortices in similar tornadoes, and spatial resolutions of ~100 m or better are needed. Since some longer-lived vortices may have been excluded from the data sample owing to the limited time window of the deployment, these durations and pathlengths are very likely underestimated.

The mean and median translational speeds of all the vortices were 59 and 55 m s^{-1}, respectively; the median is probably a better statistic to consider because outliers do not bias it as heavily. Long-lived vortices tended to move slightly more slowly (in the mean by ~11 m s^{-1}) than the short-lived secondary vortices, but the difference in the median speeds was only 4 m s^{-1}. On average,

TABLE 2. Statistics on secondary vortices. The numbers plotted without parentheses are median values, not mean values.

	Duration (s)	Distance (m)	Speed ($m\,s^{-1}$)	Origin radius (m)	Dissipation radius (m)	Change in radius (m)
All subvortices (std dev, σ)	18 (18)	969 (950)	55 (23)	641 (219)	564 (286)	−84 (262)
Long-lived subvortices (std dev, σ)	34 (19)	1818 (1112)	52 (10)	655 (110)	396 (252)	−259 (282)
Short-lived subvortices (std dev, σ)	8 (2)	470 (196)	56 (26)	632 (267)	554 (264)	29 (175)

the vortices began 641 m from the center of the parent tornado circulation and ended 564 m from the center; the average inward radial motion was only 84 m. However, by separating the vortices by longevity, it was observed that short-lived vortices, on average, moved 29 m radially outward, whereas long-lived vortices moved 259 m radially inward. Whether this difference is a cause or an effect of the longevity of the vortices is unknown.

To determine the location of the secondary vortices with respect to features in the mean circulation of the parent tornado (i.e., the mean, ''background'' flow), the medians of the Doppler velocity and spectrum width fields in the reference frame of the moving parent tornado were calculated. The vortices were located mainly within the RMW, which was ~800 m from the center of the parent circulation (Figs. 7, 9). All long-lived vortices in the two right quadrants were within the RMW. Most of the long-lived vortices tracked about halfway between the RMW and the center of the parent circulation in the right two quadrants. Any vortices that were located beyond the RMW did not persist long.

The composite (median) spectrum width field over the entire D3 time period displayed an oblate, asymmetric ring of enhanced spectrum width within the RMW, with an apparent ''break'' (i.e., weakness) in the ring at the end (with respect to a counterclockwise turning) of the left-front quadrant and the beginning of the left-rear quadrant (Fig. 11b). The ring of enhanced spectrum width was nearly collocated with the tracks of the secondary vortices and could be related to the enhanced spectrum width associated with each secondary vortex and/or to the relatively large gradients in Doppler velocity within the RMW.

Since the time series of the spectrum width field during D3 exhibited unsteady evolution as the tornado transitioned from a single-vortex structure into a multiple-vortex structure, D3 was subdivided into two parts: the first part for the first four volume scans (representing a period of predominately single-vortex structure) and the second part for the last four volume scans (representing a period of predominately multiple-vortex structure).

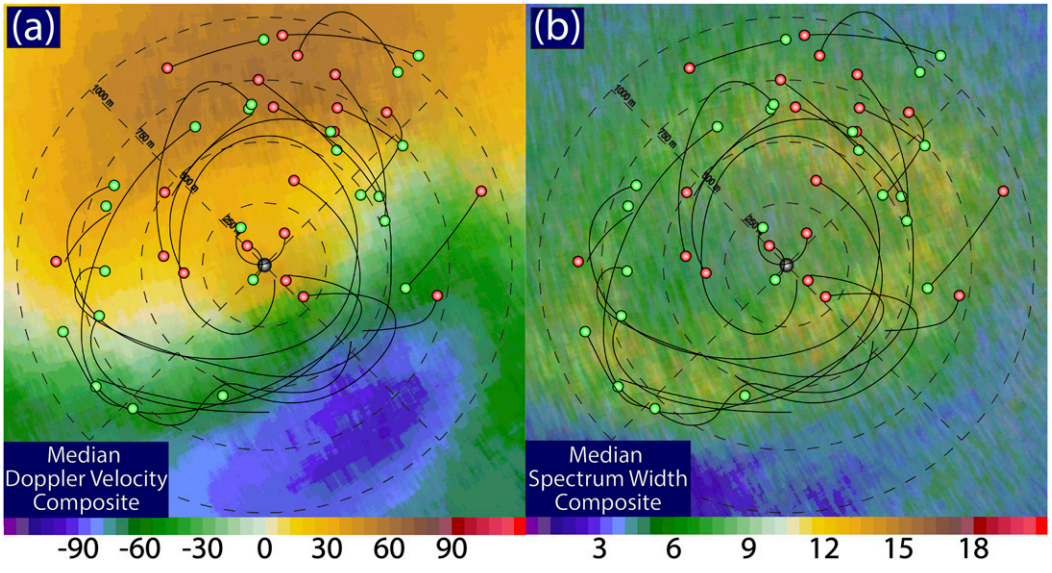

FIG. 11. Composites of (a) the median dealiased Doppler velocity ($m\,s^{-1}$) and (b) spectrum width ($m\,s^{-1}$) from RaXPol during D3. The tracks of secondary vortices from Fig. 6b are superimposed on the aforementioned two fields.

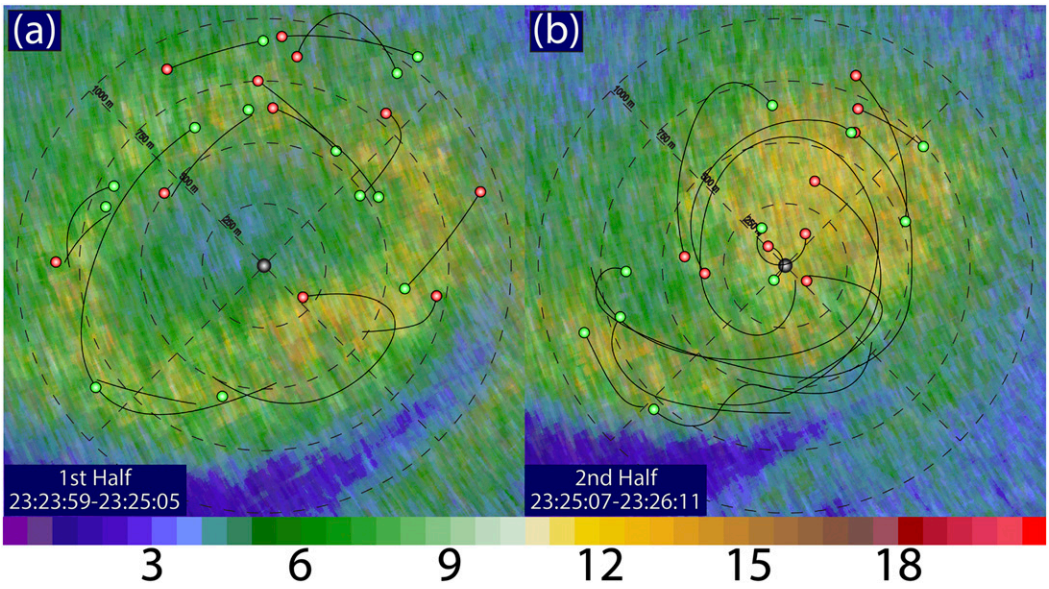

FIG. 12. As in Fig. 11b, but (a) just for the first four volumes of D3 (2323:59–2325:05 UTC) and (b) just for the last four volumes of D3 (2325:07–2326:11 UTC).

During the single-vortex period, there was an elliptical ring of enhanced spectrum width (Fig. 12a), similar to what is seen in Fig. 11b, but the ring is better defined and does not have as pronounced a break in it. The tracks of the secondary vortices were located mainly along or within this ring. However, during the later multiple-vortex period, the spectrum width field took on the appearance of a concentrated circular area of enhanced spectrum width, with greater spectrum width in the left-front and part of the right-front quadrants. A "tail" of enhanced spectrum width curled radially outward in an anticyclonic (i.e., clockwise) manner into the left-rear quadrant (Fig. 12b); looking at it from a different perspective, the band curled radially inward in a cyclonic manner from the left-rear quadrant. Like the tracks in the earlier period, the tracks of the secondary vortices were located mainly within the regions of enhanced spectrum width. Low spectrum width, in a median sense, was located outside the RMW in the right-rear quadrant, perhaps indicative of flow within the rear-flank downdraft (Skinner 2014).

As noted earlier, from laboratory models and theoretical work (e.g., Ward 1972; Rotunno 1984; Lewellen et al. 1997), it has been found that secondary vortices retrograde with respect to the parent tornado's circulation. Furthermore, Wurman (2002) found some evidence for this behavior in another multiple-vortex tornado. To compare the speeds of the secondary vortices to those of the azimuthal winds in the parent tornado circulation, a Rankine-combined vortex and a Burgers–Rott vortex (Burgers 1948; Davies-Jones 1986) were crudely fit to the composite median Doppler velocity field (by assuming that the maximum Doppler velocity was at the observed RMW) for D3 (Fig. 9a) and by assuming that the mean vortex was azimuthally symmetric. The former consists of a field of solid-body rotation surrounded by potential flow, while the latter is similar; owing to horizontal diffusion, a Burgers–Rott vortex has a smooth transition from a solid-body rotation to potential flow at the RMW. Both vortex models are specified to have an azimuthal velocity of $81.5\,\mathrm{m\,s^{-1}}$ (the average magnitude of the maximum and minimum in radial velocity found in the composite Doppler velocity field; 62.5 and $-100.5\,\mathrm{m\,s^{-1}}$, respectively; Fig. 9a) at the RMW, which is approximately 800 m. All of the long-lived vortices moved more slowly than the azimuthal winds in the fitted Burgers–Rott vortex, but only about half of them did with respect to the fitted Rankine-combined vortex (Fig. 9b). These results are similar to those found by Wurman (2002), but, in the case of the El Reno tornado, the retrogression speeds were slower or even negligible.

Our simplified analysis subtracts (adds) $\sim 20\,\mathrm{m\,s^{-1}}$ from (to) the ground-relative Doppler velocity fields to compute the mean Doppler wind field. If motion toward the radar of $10\,\mathrm{m\,s^{-1}}$ is accounted for [so the mean maximum outbound (inbound) Doppler wind speeds were 70 (90) $\mathrm{m\,s^{-1}}$] and a rear-front gust front enhancement of $10\,\mathrm{m\,s^{-1}}$ is also accounted for [so the mean maximum outbound (inbound) Doppler wind speeds were 70 (80) $\mathrm{m\,s^{-1}}$], then the maximum azimuthal wind in the symmetric parent circulation may have been

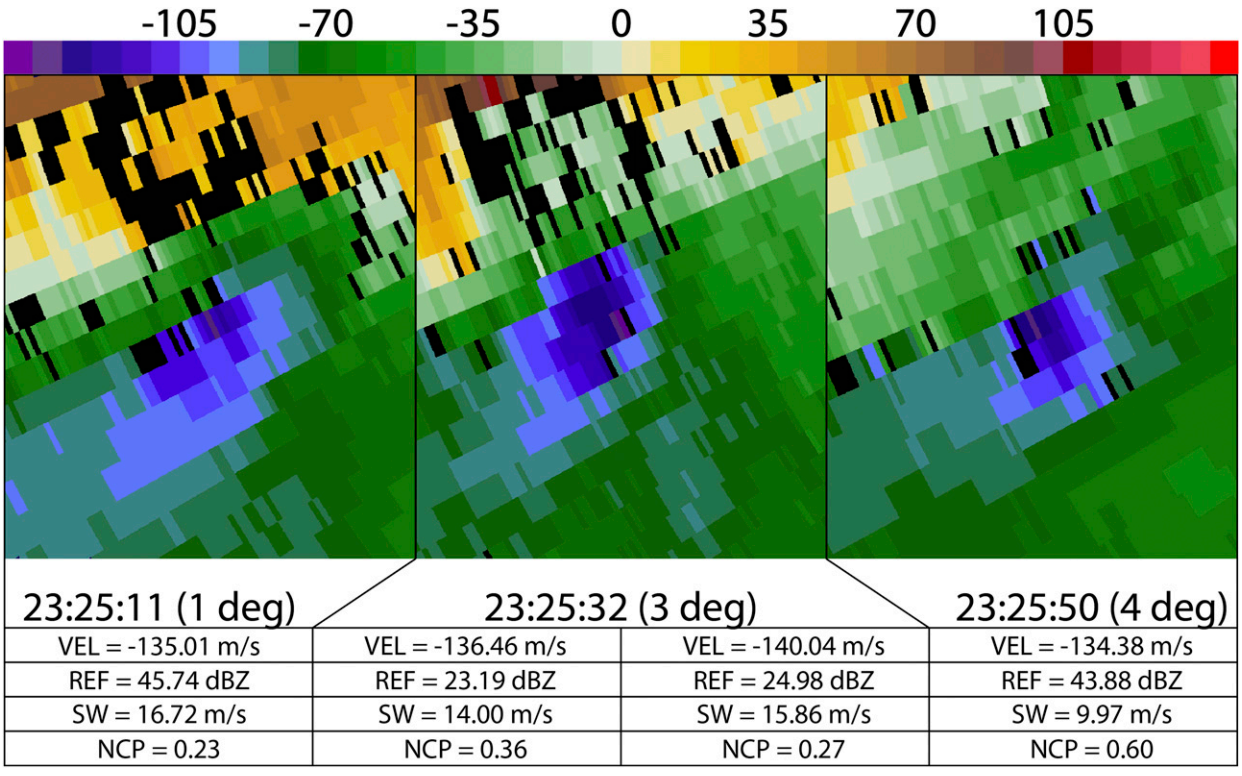

FIG. 13. Dealiased Doppler velocity ($m\,s^{-1}$) from RaXPol when the three highest wind speeds ($>130\,m\,s^{-1}$) were estimated. The times (UTC) on 31 May 2013, the elevation angle in degrees, the estimated Doppler velocity, the radar reflectivity factor, the spectrum width, and the NCP all associated with the range gate at which the Doppler velocity estimates were made, are shown.

only $70\,m\,s^{-1}$. With this analysis, fewer secondary vortices moved more slowly than the mean flow (not shown), so there is no strong evidence that the secondary vortices actually propagated against the mean flow. The azimuthal speeds of the secondary vortices varied by only $5\,m\,s^{-1}$ among the quadrants; the slowest average azimuthal speed of $50.6\,m\,s^{-1}$ was found in the right-rear quadrant, and the fastest azimuthal wind speed of $56.1\,m\,s^{-1}$ was found in the left-forward quadrant (not shown). Owing to the asymmetry in the Doppler velocity field and uncertainties in the motion of the parent vortex and the effect of the rear-flank gust front, however, our conclusions must be regarded as highly tentative.

The ground-relative wind speeds in the secondary vortices were extremely high (Wurman et al. 2014; Snyder and Bluestein 2014), owing in large part to their very high translational speed. At the beginning of D3, the tornado motion was negligible, and, based on damage surveys, the tornado followed a trochoidal loop (Wakimoto et al. 2015). After the nearly stationary period, the tornado accelerated with a component of motion in the direction of the radar of $18\,m\,s^{-1}$. The small vortex tracked in Fig. 2 translated ~700 m in 9 s, which makes the translation speed relative to the ground $\sim 78\,m\,s^{-1}$.

The highest ground-relative wind speeds recorded by RaXPol were measured in secondary vortices at 2325:32 UTC (Fig. 13): estimates of inbound wind speeds of 136.5 and $140\,m\,s^{-1}$ were found on the southeastern (i.e., right) periphery of a vortex moving through the southeastern part of the tornado. Owing to uncertainty/ambiguity in the subjective dealiasing procedure, however, our confidence in these estimates is limited. Greater spatial resolution (e.g., smaller half-power beamwidth and/or shorter range from the radar to the tornado) would have allowed us to better resolve this vortex and (other) small vortices, which would have increased our confidence in the manual dealiasing procedure and likely would have resulted in even larger peak, quasi-instantaneous velocity observations.

Our uncertainty is much lower for measurements near the surface of inbound ground-relative wind speeds of $135\,m\,s^{-1}$ because there was only one reasonable solution to the dealiased velocities in this secondary vortex at this time. For this measurement, the spectrum width was $\pm 16.7\,m\,s^{-1}$. The next highest wind speed measurement was inbound at $134.4\,m\,s^{-1}$, with a spectrum width of $\pm 10\,m\,s^{-1}$. For the latter measurement, the NCP was 0.6, while it was only 0.23 for the former

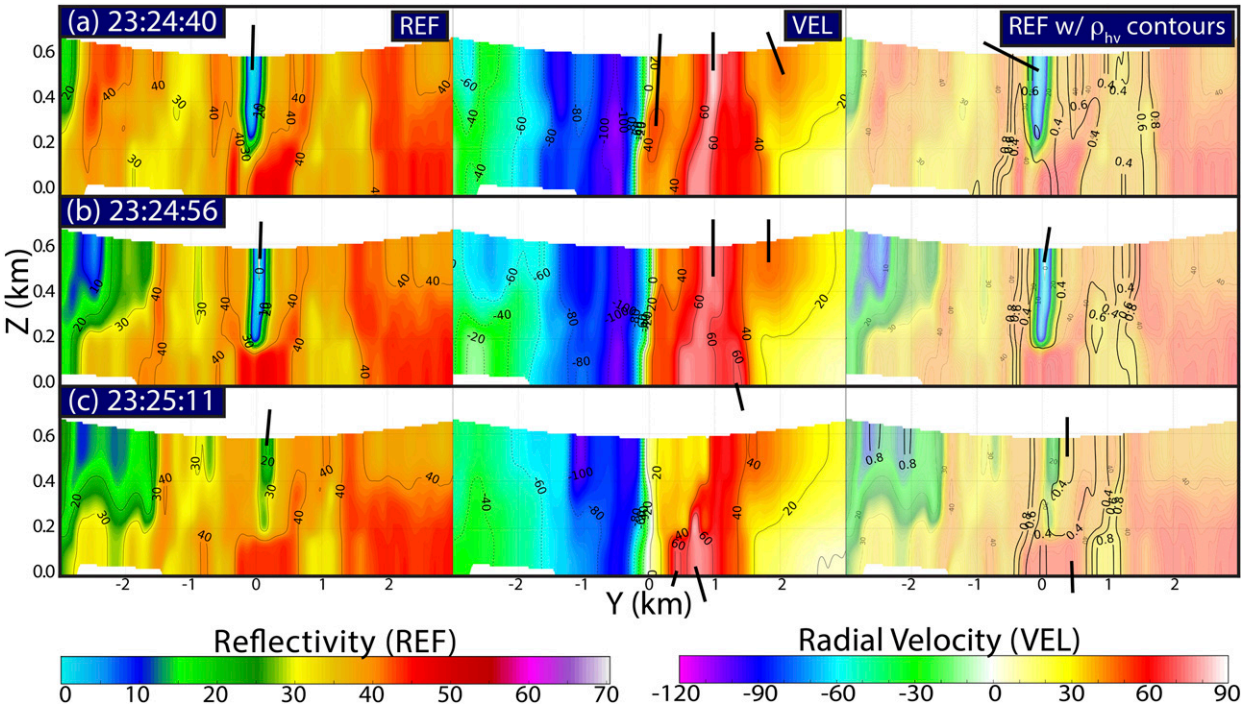

FIG. 14. Reconstructed vertical cross sections through the El Reno tornado up to 800 m above radar level (ARL), when the tornado was breaking down into a multiple-vortex structure, during D3. (left) RaXPol radar reflectivity (dBZ); (middle) dealiased Doppler velocity ($m\,s^{-1}$); (right) and reflectivity overlaid with contours of ρ_{hv} at intervals of 0.2. Areas in the center of the cross sections with $\rho_{hv} < 0.9$ represent the tornado debris signature. The WEH, relative maxima in Doppler velocity, and regions of $\rho_{hv} < 0.4$ are indicated by solid line segments; $Z = 0$ is actually the level of the radar antenna, not the ground.

measurement. All of these wind speed estimates are comparable to the 135 $m\,s^{-1}$ wind speeds measured by Wurman et al. (2007a) in the Bridge Creek–Moore tornado of 3 May 1999, but the measurements in the 3 May 1999 tornado were apparently not in a secondary vortex. Our estimate agrees with that of Wurman et al. (2014) for another secondary vortex located in the northeastern part of the parent tornado.

The vertical characteristics of the parent tornado at low altitude as it began to change from a primarily single-vortex to a multiple-vortex structure are illustrated in vertical cross sections at constant range through the approximate center at three times during D3 (Fig. 14). A WEC is found above 200 m AGL. If the WEC is caused by the radially outward centrifuging of hydrometeors and debris (e.g., Dowell et al. 2005; Tanamachi et al. 2012), then its absence below 200 m may be due to the dominance of frictionally induced radial inflow (e.g., Bluestein et al. 2004b, 2007a). However, there is not much evidence of strong tornado-relative radial inflow in the radial velocity data in this layer (e.g., below 200 m).

The WEC began to get narrower at 2325:11 UTC, during the transition to a multiple-vortex tornado. Since at and after this time the Doppler velocity field is no longer in any quasi-steady state throughout the duration of the volume scan, the vertical cross sections are not representative of the mean background tornadic wind field; Doppler velocities could be enhanced locally as secondary vortices pass through the plane of the vertical cross sections. The Doppler velocity field is asymmetric: the inbound Doppler wind field exhibits a single maximum around 750 m to the southeast of the tornado center, while the outbound wind field exhibits more than one maximum. In the minute-and-a-half spanning the observations shown in Fig. 14, there are three maxima initially, the outer of which is above 500 m. The inner one merges with the middle one, and another one appears at low altitudes. Finally, only two are discernible, while the outer one aloft begins to merge with the second, primary maximum. At all three times shown, there is some tilt radially outward (with respect to the central axis) with height. The outbound wind maxima represent inflow jets, which extend radially outward beyond the core radius of 800 m. In fact, instantaneously, the core radius cannot be determined at all. Regions of low (<0.8) copolar cross-correlation coefficient, indicative of debris, are asymmetrically distributed around the

tornado, with the lowest values found on the outbound velocity side of the tornado, where the maximum wind speeds are also found. Details of the behavior of the debris field are discussed elsewhere (Wakimoto et al. 2015).

Attempts to estimate the swirl ratio, to see if it had increased during the transition from a single-vortex tornado to a multiple-vortex tornado, as described by Davies-Jones (1986), were not successful owing to great uncertainties in determining the mean azimuthal and radial wind fields. Furthermore, Lewellen et al. (2000) found from large-eddy simulations of highly idealized vortices that parameters other than the swirl ratio, such as the surface roughness and the vertical profile of inflow velocity, also influence whether or not a tornado supports secondary vortices.

5. Summary and conclusions

This study of secondary vortices in a tornado is arguably the most comprehensive to date, using data collected every 2 s to study 24 vortices. The analysis made use of shallow volume scans (0°–5° in elevation) collected every 15–16 s during a several-minute segment of extensive data collection in a very large, unusually intense, multiple-vortex tornado. This study is just one part of a set of studies of the tornado: the formation of the tornado and other aspects of the tornado's evolution will be discussed elsewhere.

The longest-lived vortices, a few of which lasted a minute or more, tended to form near and within the RMW, in an environment of relatively strong tornado-relative radial shear of the azimuthal wind [$\sim 80\,\mathrm{m\,s^{-1}}$ $(800\,\mathrm{m})^{-1}$]. This finding is in accord with the hypothesis that shearing instability accounts for their formation. It is not known, however, how the vertical gradient of the radial wind varied, which is thought also to play a role in producing secondary vortices. Most formed in the left-rear quadrant and tracked around the center of the parent tornado and had a radially inward component of motion. The relative motion of the secondary vortices radially inward within the RMW could be due to advection by radial inflow in the boundary layer or to "beta drift" (Kuo 1969; Fiorino and Elsberry 1989; Wang and Li 1992) above the boundary layer. The secondary vortices tended to dissipate in the right-front and left-front quadrants. Some evidence was found that they propagated against the mean flow, but there were too many uncertainties connected with the process of estimating the mean flow to have much confidence in this finding.

The beginning of the period when "long-lived" vortices formed in the left-rear quadrant may be related to the appearance of small-scale waves (~400-m wavelength) in the radar reflectivity and Doppler velocity fields on the outbound side of the vortex at approximately this time. The secondary vortices then tracked around to the southeastern (inbound) side of the tornado, following a similar tornado-relative trajectory. The long-lived vortices also had a component of motion toward the center of the tornado, perhaps owing to the effects of surface friction or beta drift. They may have accelerated on the right quadrants owing to advection by a strong rear-flank gust front. Both the translational speed of the parent tornado and the rear-flank gust front probably contributed to extremely high ground-relative wind speeds in excess of $130\,\mathrm{m\,s^{-1}}$.

Future studies of secondary vortices are needed with rapid-scan Doppler radars to see if our results can be replicated in other tornadoes. A better method for determining the mean background flow of the parent tornado for secondary vortices needs to be devised and employed. The existing GBVTD technique might be more viable with a tornado that exhibits much more axisymmetry than the El Reno tornado described herein. However, caveats must be applied when using this technique because the vertical velocity field may be contaminated by debris motion. Finally, we note that instability theories have been proposed for axisymmetric flows, while the flow in the El Reno tornado was markedly nonaxisymmetric. Perhaps more attention should be given to stability analyses in highly nonaxisymmetric flow.

Acknowledgments. This study was supported by NSF Grants AGS-1262048 and AGS-1560945. RaXPol was built with MRI Grant NSF AGS-0821231. RaXPol is supported by the Advanced Radar Research Center (ARRC) at the University of Oklahoma (OU). We are indebted to John Meier, Tian Yu, and Bob Palmer at the ARRC for their radar support. The authors recognize constructive suggestions from David Nolan (University of Miami) and Lou Wicker (NSSL) during the course of this work.

APPENDIX

Algorithm for Editing Noisy Data

First, data were removed if the change in specific differential phase Φ_{DP} was between 100° and 250° between adjacent range gates and if the received power from both horizontal and vertical channels was less than −70 dBm, Then, there was a five-step iterative process of first applying a threshold of increasing NCP, followed by the successive application of a despeckling

filter with decreasing size of a defined "speckle"; NCP from 0.1 to 0.3, in increments of 0.05, along with speckle sizes of 10, five, three, two, and one range gate(s), respectively, were used. The algorithm was first used to remove areas of obvious noise and then used gradually to remove noisy areas that were blended in with less noisy data.

REFERENCES

Alexander, C. R., 2010: A mobile radar based climatology of supercell tornado structures and dynamics. Ph. D. thesis, School of Meteorology, University of Oklahoma, 229 pp.

——, and J. Wurman, 2005: The 30 May 1998 Spencer, South Dakota, storm. Part I: The structural evolution and environment of the tornadoes. *Mon. Wea. Rev.*, **133**, 72–97, https://doi.org/10.1175/MWR-2855.1.

——, and ——, 2008: Updated mobile radar climatology of supercell tornado structures and dynamics. *24th Conf. on Severe Local Storms*, Savannah, GA, Amer. Meteor. Soc., 19.4, https://ams.confex.com/ams/24SLS/techprogram/paper_141821.htm.

Beck, J., and C. Weiss, 2013: An assessment of low-level baroclinity and vorticity within a simulated supercell. *Mon. Wea. Rev.*, **141**, 649–669, https://doi.org/10.1175/MWR-D-11-00115.1.

Bluestein, H. B., 2013: *Severe Convective Storms and Tornadoes: Observations and Dynamics.* Springer, 456 pp.

——, and A. L. Pazmany, 2000: Observations of tornadoes and other convective phenomena with a mobile, 3-mm wavelength, Doppler radar: The spring 1999 field experiment. *Bull. Amer. Meteor. Soc.*, **81**, 2939–2952, https://doi.org/10.1175/1520-0477(2000)081<2939:OOTAOC>2.3.CO;2.

——, C. C. Weiss, and A. L. Pazmany, 2004a: Doppler radar observations of dust devils in Texas. *Mon. Wea. Rev.*, **132**, 209–224, https://doi.org/10.1175/1520-0493(2004)132<0209:DROODD>2.0.CO;2.

——, ——, and ——, 2004b: The vertical structure of a tornado near Happy, Texas, on 5 May 2002: High-resolution, mobile, W-band, Doppler radar observations. *Mon. Wea. Rev.*, **132**, 2325–2337, https://doi.org/10.1175/1520-0493(2004)132<2325:TVSOAT>2.0.CO;2.

——, ——, M. M. French, E. M. Holthaus, R. L. Tanamachi, S. Frasier, and A. L. Pazmany, 2007a: The structure of tornadoes near Attica, Kansas, on 12 May 2004: High-resolution, mobile, Doppler radar observations. *Mon. Wea. Rev.*, **135**, 475–506, https://doi.org/10.1175/MWR3295.1.

——, M. M. French, R. L. Tanamachi, S. Frasier, K. Hardwick, F. Junyent, and A. L. Pazmany, 2007b: Close-range observations of tornadoes in supercells made with a dual-polarization, X-band, mobile Doppler radar. *Mon. Wea. Rev.*, **135**, 1522–1543, https://doi.org/10.1175/MWR3349.1.

——, ——, I. PopStefanija, R. T. Bluth, and J. B. Knorr, 2010: A mobile, phased-array Doppler radar for the study of severe convective storms: The MWR-05XP. *Bull. Amer. Meteor. Soc.*, **91**, 579–600, https://doi.org/10.1175/2009BAMS2914.1.

——, J. C. Snyder, and J. B. Houser, 2015: A multiscale overview of the El Reno, Oklahoma, tornadic supercell of 31 May 2013. *Wea. Forecasting*, **30**, 525–552, https://doi.org/10.1175/WAF-D-14-00152.1.

Bringi, V. N., and V. Chandrasekar, 2001: *Polarimetric Doppler Weather Radar.* 1st ed. Cambridge University Press, 636 pp.

Burgers, J. M., 1948: A mathematical model illustrating the theory of turbulence. *Adv. Appl. Mech.*, **1**, 171–199, https://doi.org/10.1016/S0065-2156(08)70100-5.

Church, C. R., J. T. Snow, G. L. Baker, and E. M. Agee, 1979: Characteristics of tornado-like vortices as a function of swirl ratio: A laboratory investigation. *J. Atmos. Sci.*, **36**, 1755–1776, https://doi.org/10.1175/1520-0469(1979)036<1755:COTLVA>2.0.CO;2.

Dahl, N. A., D. S. Nolan, G. H. Bryan, and R. Rotunno, 2017: Using high-resolution simulations to quantify underestimates of tornado intensity from in situ observations. *Mon. Wea. Rev.*, **145**, 1963–1982, https://doi.org/10.1175/MWR-D-16-0346.1.

Davies-Jones, R. P., 1973: The dependence of core radius on swirl ration in a tornado simulator. *J. Atmos. Sci.*, **30**, 1427–1430, https://doi.org/10.1175/1520-0469(1973)030<1427:TDOCRO>2.0.CO;2.

——, 1986: Tornado dynamics. *Thunderstorm Morphology and Dynamics*, E. Kessler, Ed., University of Oklahoma Press, 197–236.

——, R. J. Trapp, and H. B. Bluestein, 2001: Tornadoes and tornadic storms. *Severe Convective Storms*, *Meteor. Monogr.*, No. 50, Amer. Meteor. Soc., 167–221, https://doi.org/10.1175/0065-9401-28.50.167.

Doviak, R. J., and D. S. Zrnić, 1993: *Doppler Radar and Weather Observations.* 2nd ed. Academic Press, 562 pp.

Dowell, D. C., C. R. Alexander, J. M. Wurman, and L. J. Wicker, 2005: Centrifuging of hydrometeors and debris in tornadoes: Radar-reflectivity patterns and wind-measurement errors. *Mon. Wea. Rev.*, **133**, 1501–1524, https://doi.org/10.1175/MWR2934.1.

Fiorino, M., and R. L. Elsberry, 1989: Some aspects of vortex structure related to tropical cyclone motion. *J. Atmos. Sci.*, **46**, 975–990, https://doi.org/10.1175/1520-0469(1989)046<0975:SAOVSR>2.0.CO;2.

Forbes, G. S., 1978: Three scales of motion associated with tornadoes. Final Rep. to U.S. Nuclear Regulatory Commission NUREG/CR-0363, 359 pp.

Friedrich, K., and O. Caumont, 2004: Dealiasing Doppler velocities measured by a bistatic radar network during a downburst-producing thunderstorm. *J. Atmos. Oceanic Technol.*, **21**, 717–729, https://doi.org/10.1175/1520-0426(2004)021<0717:DDVMBA>2.0.CO;2.

——, and M. Hagen, 2004: Evaluation of wind vectors measured by a bistatic Doppler radar network. *J. Atmos. Oceanic Technol.*, **21**, 1840–1854, https://doi.org/10.1175/JTECH-1679.1.

——, ——, and T. Einfalt, 2006: A quality control concept for radar reflectivity, polarimetric parameters, and Doppler velocity. *J. Atmos. Oceanic Technol.*, **23**, 865–887, https://doi.org/10.1175/JTECH1920.1.

Fujita, T. T., 1981: Tornadoes and downbursts in the context of generalized planetary scales. *J. Atmos. Sci.*, **38**, 1511–1534, https://doi.org/10.1175/1520-0469(1981)038<1511:TADITC>2.0.CO;2.

——, D. L. Bradbury, and C. F. Van Thullenar, 1970: Palm Sunday tornadoes of April 11, 1965. *Mon. Wea. Rev.*, **98**, 29–69, https://doi.org/10.1175/1520-0493(1970)098<0029:PSTOA>2.3.CO;2.

Houser, J. L., H. B. Bluestein, and J. C. Snyder, 2016: A finescale radar examination of the tornadic debris signature and weak-echo reflectivity band associated with a large, violent tornado. *Mon. Wea. Rev.*, **144**, 4101–4130, https://doi.org/10.1175/MWR-D-15-0408.1.

Kosiba, K. A., and J. Wurman, 2013: The three-dimensional structure and evolution of a tornado boundary layer. *Wea. Forecasting*, **28**, 1552–1561, https://doi.org/10.1175/WAF-D-13-00070.1.

——, ——, Y. Richardson, P. Markowski, P. Robinson, and J. Marquis, 2013: Genesis of the Goshen County, Wyoming, tornado on 5 June 2009 during VORTEX2. *Mon. Wea. Rev.*, **141**, 1157–1181, https://doi.org/10.1175/MWR-D-12-00056.1.

Kuo, H. L., 1969: Motions of vortices and circulating cylinder in shear flow with friction. *J. Atmos. Sci.*, **26**, 390–398, https://doi.org/10.1175/1520-0469(1969)026<0390:MOVACC>2.0.CO;2.

Kurdzo, J. M., D. J. Bodine, B. L. Cheong, and R. D. Palmer, 2015: High-temporal resolution polarimetric X-band Doppler radar observations of the 20 May 2013 Moore, Oklahoma, tornado. *Mon. Wea. Rev.*, **143**, 2711–2735, https://doi.org/10.1175/MWR-D-14-00357.1.

——, and Coauthors, 2017: Observations of severe local storms and tornadoes with the Atmospheric Imaging Radar. *Bull. Amer. Meteor. Soc.*, **98**, 915–935, https://doi.org/10.1175/BAMS-D-15-00266.1.

Lee, W.-C., and J. Wurman, 2005: Diagnosed three-dimensional axisymmetric structure of the Mulhall tornado on 3 May 1999. *J. Atmos. Sci.*, **62**, 2373–2393, https://doi.org/10.1175/JAS3489.1.

——, B. J.-D. Jou, P.-L. Chang, and S.-M. Deng, 1999: Tropical cyclone kinematic structure retrieved from single-Doppler radar observations. Part I: Interpretation of Doppler velocity patterns and the GBVTD technique. *Mon. Wea. Rev.*, **127**, 2419–2439, https://doi.org/10.1175/1520-0493(1999)127<2419:TCKSRF>2.0.CO;2.

Lewellen, D. C., W. S. Lewellen, and J. Xia, 2000: The influence of a local swirl ratio on tornado intensification near the surface. *J. Atmos. Sci.*, **57**, 527–544, https://doi.org/10.1175/1520-0469(2000)057<0527:TIOALS>2.0.CO;2.

Lewellen, W. S., 1962: A solution for three-dimensional vortex flows with strong circulation. *J. Fluid Mech.*, **14**, 420–432, https://doi.org/10.1017/S0022112062001330.

——, D. C. Lewellen, and R. I. Sykes, 1997: Large-eddy simulation of a tornado's interaction with the surface. *J. Atmos. Sci.*, **54**, 581–605, https://doi.org/10.1175/1520-0469(1997)054<0581:LESOAT>2.0.CO;2.

Markowski, P., and Coauthors, 2012: The pretornadic phase of the Goshen County, Wyoming, supercell of 5 June 2009 intercepted by VORTEX2. Part I: Evolution of kinematic and surface thermodynamic fields. *Mon. Wea. Rev.*, **140**, 2887–2915, https://doi.org/10.1175/MWR-D-11-00336.1.

Marquis, J., Y. Richardson, P. Markowski, D. Dowell, and J. Wurman, 2012: Tornado maintenance investigated with high-resolution dual-Doppler and EnKF analysis. *Mon. Wea. Rev.*, **140**, 3–27, https://doi.org/10.1175/MWR-D-11-00025.1.

Moon, Y., and D. S. Nolan, 2015: Spiral rainbands in a numerical simulation of Hurricane Bill (2009). Part II: Propagation of inner rainbands. *J. Atmos. Sci.*, **72**, 191–215, https://doi.org/10.1175/JAS-D-14-0056.1.

Nolan, D. S., 2012: Three-dimensional instabilities in tornado-like vortices with secondary circulations. *J. Fluid Mech.*, **711**, 61–100, https://doi.org/10.1017/jfm.2012.369.

——, 2013: On the use of Doppler radar–derived wind fields to diagnose the secondary circulations of tornadoes. *J. Atmos. Sci.*, **70**, 1160–1171, https://doi.org/10.1175/JAS-D-12-0200.1.

Oye, R., C. Mueller, and S. Smith, 1995: Software for radar translation, visualization, editing, and interpolation. *27th Conf. on Radar Meteorology*, Vail, CO, Amer. Meteor. Soc., 359–361.

Pazmany, A. L., J. B. Mead, H. B. Bluestein, J. C. Snyder, and J. B. Houser, 2013: A mobile rapid-scanning X-band polarimetric (RaXPol) Doppler radar system. *J. Atmos. Oceanic Technol.*, **30**, 1398–1413, https://doi.org/10.1175/JTECH-D-12-00166.1.

Potvin, C. K., 2013: A variational method for detecting and characterizing convective vortices in Cartesian wind fields. *Mon. Wea. Rev.*, **141**, 3102–3115, https://doi.org/10.1175/MWR-D-13-00015.1.

Rankine, W. J. M., 1882: *A Manual of Applied Physics*. 10th ed. Charles Griffin and Co., 663 pp.

Reasor, P. D., M. T. Montgomery, F. D. Marks Jr., and J. F. Gamache, 2000: Low-wavenumber structure and evolution of the hurricane inner core observed by airborne dual-Doppler radar. *Mon. Wea. Rev.*, **128**, 1653–1680, https://doi.org/10.1175/1520-0493(2000)128<1653:LWSAEO>2.0.CO;2.

Rotunno, R., 1978: A note on the stability of a cylindrical vortex sheet. *J. Fluid Mech.*, **87**, 761–771, https://doi.org/10.1017/S0022112078001871.

——, 1984: An investigation of a three-dimensional asymmetric vortex. *J. Atmos. Sci.*, **41**, 283–298, https://doi.org/10.1175/1520-0469(1984)041<0283:AIOATD>2.0.CO;2.

——, 2013: The fluid dynamics of tornadoes. *Annu. Rev. Fluid Mech.*, **45**, 59–84, https://doi.org/10.1146/annurev-fluid-011212-140639.

Ryzhkov, A. V., T. J. Schuur, D. W. Burgess, and D. S. Zrnic, 2005: Polarimetric tornado detection. *J. Appl. Meteor.*, **44**, 557–570, https://doi.org/10.1175/JAM2235.1.

Schroth, A. C., M. S. Chandra, and P. F. Mesichner, 1988: A *C*-band coherent polarimetric radar for propagation and cloud physics research. *J. Atmos. Oceanic Technol.*, **5**, 803–822, https://doi.org/10.1175/1520-0426(1988)005<0803:ABCPRF>2.0.CO;2.

Schubert, W. H., M. T. Montgomery, R. K. Taft, F. A. Guinn, S. R. Fulton, J. P. Kossin, and J. P. Edwards, 1999: Polygonal eyewalls, asymmetric eye contraction, and potential vorticity mixing in hurricanes. *J. Atmos. Sci.*, **56**, 1197–1223, https://doi.org/10.1175/1520-0469(1999)056<1197:PEAECA>2.0.CO;2.

Seimon, A., J. T. Allen, T. A. Seimon, S. J. Talbot, and D. K. Hoadley, 2016: Crowdsourcing the El Reno 2013 tornado: A new approach for collation and display of storm chaser imagery for scientific applications. *Bull. Amer. Meteor. Soc.*, **97**, 2069–2084, https://doi.org/10.1175/BAMS-D-15-00174.1.

Skinner, P. S., 2014: Observations and ensemble Kalman filter analyses of multiple internal rear-flank downdraft momentum surges within the 18 May 2010, Dumas, Texas supercell. Ph.D. dissertation, Texas Tech University, 182 pp., https://ttu-ir.tdl.org/ttu-ir/handle/2346/58709.

——, C. C. Weiss, M. M. French, H. B. Bluestein, P. M. Markowski, and Y. P. Richardson, 2014: VORTEX2 observations of a low-level mesocyclone with multiple internal rear-flank downdraft momentum surges in the 18 May 2010 Dumas, Texas, supercell. *Mon. Wea. Rev.*, **142**, 2935–2960, https://doi.org/10.1175/MWR-D-13-00240.1.

Snyder, J. C., and H. B. Bluestein, 2014: Some considerations for the use of high-resolution mobile radar data in tornado intensity determination. *Wea. Forecasting*, **29**, 799–827, https://doi.org/10.1175/WAF-D-14-00026.1.

Staley, D. O., and R. L. Gall, 1979: Barotropic instability in a tornado vortex. *J. Atmos. Sci.*, **36**, 973–981, https://doi.org/10.1175/1520-0469(1979)036<0973:BIIATV>2.0.CO;2.

Tanamachi, R. L., H. B. Bluestein, W.-C. Lee, M. Bell, and A. Pazmany, 2007: Ground-based velocity track display (GBVTD) analysis of W-band Doppler radar data in a tornado near Stockton, Kansas, on 15 May 1999. *Mon. Wea. Rev.*, **135**, 783–800, https://doi.org/10.1175/MWR3325.1.

——, ——, J. B. Houser, S. J. Frasier, and K. M. Hardwick, 2012: Mobile, X-band, polarimetric Doppler radar observations

of the 4 May 2007 Greensburg, Kansas, tornadic supercell. *Mon. Wea. Rev.*, **140**, 2103–2125, https://doi.org/10.1175/MWR-D-11-00142.1.

——, ——, M. Xue, W.-C. Lee, K. A. Orzel, S. J. Frasier, and R. M. Wakimoto, 2013: Near-surface vortex structure in a tornado and in a sub-tornado-strength convective-storm vortex observed by a mobile, W-band radar during VORTEX2. *Mon. Wea. Rev.*, **141**, 3661–3690, https://doi.org/10.1175/MWR-D-12-00331.1.

Terwey, W. D., and M. T. Montgomery, 2002: Wavenumber-2 and wavenumber-*m* vortex Rossby wave instabilities in a generalized three-region model. *J. Atmos. Sci.*, **59**, 2421–2427, https://doi.org/10.1175/1520-0469(2002)059<2421:WAWMVR>2.0.CO;2.

Thiem, K. J., 2016: Rapid-scan, polarimetric, mobile, Doppler-radar observations of the formation, evolution, and structure of the El Reno Tornado of 31 May 2013. M.S. thesis, School of Meteorology, University of Oklahoma, 120 pp., https://hdl.handle.net/11244/45410.

Uttal, R., and J. M. Intrieri, 1993: Comparison of cloud boundaries measured with 8.6 mm radar and 10.6 μm lidar. *Proc. IEEE Topical Symp. on Combined Optical, Microwave, Earth and Atmospheric Sensing*, Albuquerque, NM, IEEE, 207–210.

Wakimoto, R. M., and C. Liu, 1998: The Garden City, Kansas, storm during VORTEX 95. Part II: The wall cloud and tornado. *Mon. Wea. Rev.*, **126**, 393–408, https://doi.org/10.1175/1520-0493(1998)126<0393:TGCKSD>2.0.CO;2.

——, N. T. Atkins, and J. Wurman, 2011: The LaGrange tornado during VORTEX2. Part I: Photogrammeteric analysis of the tornado combined with single-Doppler radar data. *Mon. Wea. Rev.*, **139**, 2233–2258, https://doi.org/10.1175/2010MWR3568.1.

——, P. Stauffer, W.-C. Lee, N. T. Atkins, and J. Wurman, 2012: Finescale structure of the LaGrange, Wyoming, tornado during VORTEX2: GBVTD and photogrammetric analyses. *Mon. Wea. Rev.*, **140**, 3397–3418, https://doi.org/10.1175/MWR-D-12-00036.1.

——, N. T. Atkins, K. M. Butler, H. B. Bluestein, K. Thiem, J. Snyder, and J. Houser, 2015: Photogrammetric analysis of the 2013 El Reno tornado combined with mobile X-band polarimetric radar data. *Mon. Wea. Rev.*, **143**, 2657–2683, https://doi.org/10.1175/MWR-D-15-0034.1.

Walko, R., and R. Gall, 1984: A two-dimensional linear stability analysis of the multiple vortex phenomenon. *J. Atmos. Sci.*, **41**, 3456–3471, https://doi.org/10.1175/1520-0469(1984)041<3456:ATDLSA>2.0.CO;2.

Wang, B., and X. Li, 1992: The beta drift of three-dimensional vortices: A numerical study. *Mon. Wea. Rev.*, **120**, 579–593, https://doi.org/10.1175/1520-0493(1992)120<0579:TBDOTD>2.0.CO;2.

Ward, N. B., 1972: The exploration of certain features of tornado dynamics using a laboratory model. *J. Atmos. Sci.*, **29**, 1194–1204, https://doi.org/10.1175/1520-0469(1972)029<1194:TEOCFO>2.0.CO;2.

Weiss, C. C., D. C. Dowell, J. L. Schroeder, P. S. Skinner, A. E. Reinhart, P. M. Markowski, and Y. P. Richardson, 2015: A comparison of near-surface buoyancy and baroclinity across three VORTEX2 supercell intercepts. *Mon. Wea. Rev.*, **143**, 2736–2753, https://doi.org/10.1175/MWR-D-14-00307.1.

WSEC, 2006: A recommendation for an enhanced Fuiita scale (EF-scale). Texas Tech. University, Wind Science and Engineering Center Rep., 95 pp., https://www.spc.noaa.gov/faq/tornado/ef-ttu.pdf.

Wurman, J., 2002: The multiple-vortex structure of a tornado. *Wea. Forecasting*, **17**, 473–505, https://doi.org/10.1175/1520-0434(2002)017<0473:TMVSOA>2.0.CO;2.

——, and S. Gill, 2000: Finescale radar observations of the Dimmitt, Texas (2 June 1995), tornado. *Mon. Wea. Rev.*, **128**, 2135–2164, https://doi.org/10.1175/1520-0493(2000)128<2135:FROOTD>2.0.CO;2.

——, and M. Randall, 2001: An inexpensive, mobile, rapid-scan radar. Preprints, *30th Int. Conf. on Radar Meteorology*, Munich, Germany, Amer. Meteor. Soc., P3.4, https://ams.confex.com/ams/30radar/techprogram/paper_21577.

——, and K. Kosiba, 2013: Finescale radar observations of tornado and mesocyclone structures. *Wea. Forecasting*, **28**, 1157–1174, https://doi.org/10.1175/WAF-D-12-00127.1.

——, J. Straka, E. Rasmussen, M. Randall, and A. Zahrai, 1997: Design and deployment of a portable, pencil-beam, pulsed, 3-cm Doppler radar. *J. Atmos. Oceanic Technol.*, **14**, 1502–1512, https://doi.org/10.1175/1520-0426(1997)014<1502:DADOAP>2.0.CO;2.

——, C. Alexander, P. Robinson, and Y. Richardson, 2007a: Low-level winds in tornadoes and potential catastrophic tornado impacts in urban areas. *Bull. Amer. Meteor. Soc.*, **88**, 31–46, https://doi.org/10.1175/BAMS-88-1-31.

——, Y. Richardson, C. Alexander, S. Weygandt, and P. F. Zhang, 2007b: Dual-Doppler and single-Doppler analysis of a tornadic storm undergoing mergers and repeated tornadogenesis. *Mon. Wea. Rev.*, **135**, 736–758, https://doi.org/10.1175/MWR3276.1.

——, K. Kosiba, P. Robinson, and T. Marshall, 2014: The role of multiple-vortex tornado structure in causing storm researcher fatalities. *Bull. Amer. Meteor. Soc.*, **95**, 31–45, https://doi.org/10.1175/BAMS-D-13-00221.1.